

# Quantum Scattering of Fullerene $^{12}\text{C}_{60}$ with Rare Gas Atoms and its selection rules for rotational quenching

Alexander Petrov,<sup>1</sup> Anna Linnik,<sup>1</sup> Jacek Klos,<sup>1,2</sup> Eite Tiesinga,<sup>2</sup> and Svetlana Kotochigova<sup>1,\*</sup>

<sup>1</sup>*Department of Physics, Temple University, Philadelphia, Pennsylvania 19122, USA*

<sup>2</sup>*Joint Quantum Institute, National Institute of Standards and Technology  
and University of Maryland, Gaithersburg, Maryland 20899, USA*

The discovery of the  $\text{C}_{60}$  fullerene opened new horizons to design carbon nanostructures with targeted electronic structure as well as transport and optical properties. For example, endohedral  $^{12}\text{C}_{60}$  molecules were proposed as candidates for functional quantum architectures to store and manipulate encased atomic and molecular qubits. Recent advances in cryogenic buffer-gas cooling and frequency-comb spectroscopy have enabled rovibrational quantum-state-resolved measurements of gas-phase  $^{12}\text{C}_{60}$ , revealing rotational fine structure reflecting its high icosahedral symmetry. Here, we present a perturbative quantum description of the  $^{12}\text{C}_{60}$  molecule interacting with a buffer gas of  $^{40}\text{Ar}$  atoms at temperatures of order 150 K, including a detailed analysis of their electronic structure, their interaction anisotropies, and the collision-induced rotational quenching of  $^{12}\text{C}_{60}$  in its vibrational and electronic ground state. The role of the icosahedral symmetry on the collisional dynamics is emphasized leading to a complex dependence on the  $^{12}\text{C}_{60}$  rotational quantum number. Finally, we compute the isotropic and anisotropic static and dynamic dipole polarizability of  $^{12}\text{C}_{60}$  in its absolute ground state in order to evaluate the long-range, van der Waals interaction between  $^{12}\text{C}_{60}$  and  $^{40}\text{Ar}$ .

## I. INTRODUCTION

The discovery of the buckminsterfullerene,  $\text{C}_{60}$ , by Kroto *et al.* [1] in 1985 initiated physico-chemical research of this carbon allotrope and its derivatives [2, 3]. This molecule, with its highly symmetric icosahedral structure, consists of a closed cage of 12 pentagons and 20 hexagons. Since then, an extended family of fullerenes, including  $\text{C}_{70}$ ,  $\text{C}_{74}$ ,  $\text{C}_{76}$ ,  $\text{C}_{78}$ , and  $\text{C}_{80}$ , has been synthesized, each preserving the 12-pentagons, while differing in the number and arrangement of hexagons. The unprecedented properties of this family and its derivatives inspired many applications in nanocarbon chemistry, superconductivity, and optoelectronics [4].

Fullerene molecules are still regarded as an exotic molecular form of carbon, even though  $^{12}\text{C}_{60}$  with its zero nuclear spin can easily be formed in the gas phase [1] as well as in a crystal structure [5]. As fullerenes are nearly spherical in shape, they can encapsulate single atoms, such as lanthanides [6], small molecules [7–9], as well as even larger molecules [10, 11]. Recently, the hydrocarbon  $\text{CH}_4$  was placed inside  $^{12}\text{C}_{60}$  fullerenes using “molecular surgery” as pioneered by Jafari *et al.* [12]. These authors also performed terahertz spectroscopy on this endohedral fullerene. Another type of fullerene derivative is created by binding dopant atoms or molecules to the outside of a fullerene [13–15]. These derivatives are called exohedral fullerenes. Here, alkali-metal-doped fullerenes have attracted attention due to their superconductive properties [16–18]. Finally, complex-shaped carbon molecules, such as nanoballs and nanotubes, can be created [19].

Small and large carbon-containing molecules as well as clusters have been observed by astrophysicists studying

the infrared emission in the intergalactic medium [20–24]. Fullerenes in these media were first observed by Ref. [25] and modeled, for example, in Refs. [26, 27]. Molecules of the fullerene family were proposed as candidates for functional quantum architectures to store and manipulate atomic and molecular qubits in quantum computing devices [28, 29].

In the gas phase, fullerenes and their derivatives are characterized by a large number of rotational, vibrational and electronic degrees of freedom or normal modes. Recently, gas-phase  $^{12}\text{C}_{60}$  was cooled to a temperature of 150 K using buffer gas cooling [29] and high-resolution infrared spectroscopy on a vibrational band resolved hundreds of rotational transitions  $J \rightarrow J'$ . Here,  $J$  and  $J'$  are the total molecular angular momenta of the initial and final vibrational state, respectively. In a second investigation [30], these authors describe the interaction of  $^{12}\text{C}_{60}$  with atomic and inert molecular buffer gasses. They combined state-selective optical pumping on the same vibrational band of  $^{12}\text{C}_{60}$  with buffer gas collisions to observe rotational and vibrational energy transfers. The role of the icosahedral symmetry of  $^{12}\text{C}_{60}$  could be deduced from complex level repulsions in  $J - J' = 0$  transitions, the so-called P-branch [31]. Regimes with and without level repulsion as a function of  $J$  were observed, corresponding to ergodic and non-ergodic behavior, respectively. In 2025, an even colder, 30 K  $^{12}\text{C}_{60}$  sample was achieved with a helium buffer gas [32]. The authors of this experiment also tested the symmetrization postulate for 60 identical bosonic carbon atoms and its connection to spin statistics. A review of these research efforts can be found in Ref. [33].

The purpose of this article is to put forward a quantitative, quantum description of the role of the molecular icosahedral  $I_h$  symmetry of  $^{12}\text{C}_{60}$  in collisions with noble gas atoms and compute inelastic rate coefficients describ-

\* skotoch@temple.edu

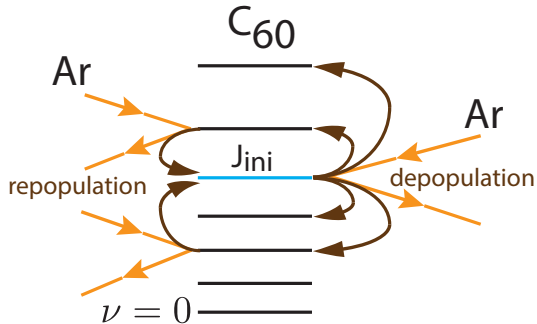


FIG. 1. Schematic of depopulation (quenching) and repopulation of rotational states (black and blue horizontal lines) of the energetically lowest vibrational state of  $^{12}\text{C}_{60}$  in collisions with argon atoms.

ing transitions among rotational states of  $^{12}\text{C}_{60}$ . Figure 1 shows the principle of these efforts. Optical pumping removes all population in a single rotational state of  $^{12}\text{C}_{60}$  in its ground vibrational level, denoted by angular momentum  $J_{\text{ini}}$ , which is then repopulated as well as depopulated in collisions with Ar rare-gas atoms. Because fullerenes have the highest possible point-group symmetry, this corresponds to partially uncharted territory in molecular collisions. We focus on  $^{40}\text{Ar}$  atoms as the collision partner and assume that  $^{12}\text{C}_{60}$  and the argon atoms are cooled to temperatures between 100 K and 200 K. At these temperatures, we need only to concentrate on the thermal population of rotational levels of the  $v = 0$  vibrational state of  $^{12}\text{C}_{60}$ . The first excited vibrational mode of  $^{12}\text{C}_{60}$  is at energy  $hc \times 273 \text{ cm}^{-1}$  or  $k \times 393 \text{ K}$  [34]. Here,  $h$  is the Planck constant,  $c$  is the speed of light in vacuum, and  $k$  is the Boltzmann constant. We find that the total collisional cross-section and rate coefficient are dominated by elastic scattering from the isotropic short- and long-range interaction potential.

In Section II, we describe our calculation of the  $\text{C}_{60}\text{-Ar}$  ground-state electronic potential energy surface (PES) and its expansion into anisotropic contributions. The allowed rotational states in gas phase  $^{12}\text{C}_{60}$  are affected by the icosahedral  $I_h$  symmetry and the fact that carbon-12 atoms are spin-zero bosons. This is discussed in Sec. III. In Sec. IV, we describe the required symmetry-adapted second-order perturbation theory to compute inelastic cross sections and rate coefficients at collision energy  $E$ . We show in Sec. V that inelastic, quenching rate coefficients of rotational levels as high as  $J = 250$  are orders of magnitude smaller than elastic rate coefficients at the same  $J$ . Moreover, we predict collisional selection rules that are different from those for molecules with lower symmetries. We summarize and conclude in Sec. VI. In Appendix A we compute the dynamic dipole polarizability of  $\text{C}_{60}$  both as function of real and imaginary frequency. The behavior as function of imaginary frequencies is used in calculations of dispersion coefficients

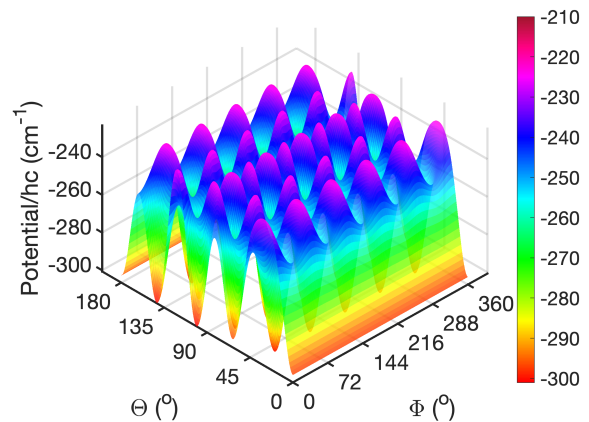


FIG. 2. Surface plot of the ground-state  $\text{C}_{60}\text{-Ar}$  potential as a function of Jacobi angles  $(\theta, \phi)$  for the equilibrium separation  $R = 13.6a_0$  between the centers of masses of  $^{12}\text{C}_{60}$  and  $^{40}\text{Ar}$ .

between fullerenes and argon atoms.

## II. ISOTROPIC AND ANISOTROPIC COMPONENTS OF THE $\text{C}_{60}\text{-AR}$ POTENTIAL ENERGY SURFACE

We start this paper by describing our *ab-initio* density functional theory (DFT) calculations using Gaussian 09 [35] employing the hybrid wB97XD functional where the long-range interactions are described using Grimme's D2 dispersion model parameter and the 6-31G(d,p) basis set. We use the counterpoise correction scheme to account for basis set superposition errors. We have chosen this functional and dispersion model as a compromise between the quality of the potential energy surface and computational time to scan on a grid of spatial geometries. See Ref. [36] for an analysis of the accuracy of different dispersion models.

We model the fullerene molecule as a rigid body with the sixty carbon atoms fixed at their equilibrium positions, so that the interaction of the noble gas atom is described by Jacobi coordinates  $(R, \theta, \phi)$ , where separation  $R$  and body-fixed angles  $\theta$  and  $\phi$  locate the center of mass of the  $^{40}\text{Ar}$  atom with respect to the center of mass of  $^{12}\text{C}_{60}$ . The polar  $\theta$  and azimuthal  $\phi$  angles are defined with respect to a right-handed Cartesian coordinate system with axes  $x$ ,  $y$ , and  $z$ , where the  $x$  and  $z$  axes coincides with a two- and five-fold symmetry axis of  $^{12}\text{C}_{60}$ , respectively. Figure 2 shows the two-dimensional cut through the PES at  $R = 13.6a_0$ , where  $a_0$  is the Bohr radius. At this separation the potential has its absolute minima at  $\approx hc \times -300 \text{ cm}^{-1}$  relative to the potential energy for  $R \rightarrow \infty$ . In fact, there are sixty equally deep minima. A depth of  $hc \times 300 \text{ cm}^{-1}$  is a rather shallow bond and is on the order of our collision energies. The anisotropic contributions, that is the  $\theta$  and  $\phi$  dependence of the PES, are relatively small of order  $hc \times 20 \text{ cm}^{-1}$ .

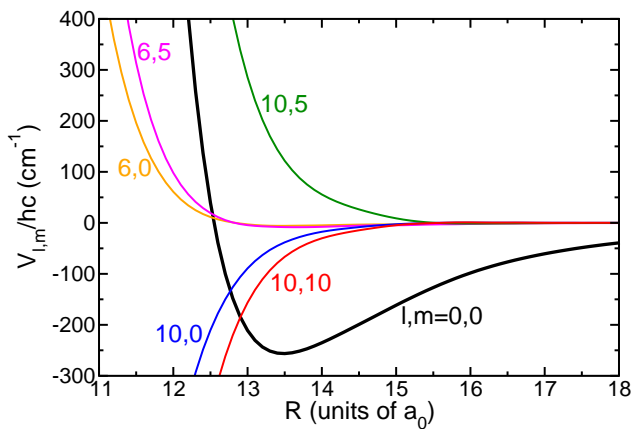


FIG. 3. Dominant non-zero radial expansion coefficients  $V_{l,m}(R)$  of  $C_{60}$ -Ar as functions of the separation between the centers of masses of  $C_{60}$  and Ar. Reproduced with permission from Ref. [30].

For separations  $R < 12.5a_0$ , not shown in the figure, the PES is repulsive.

For scattering computations, we rewrite the PES for  $C_{60}$ -Ar as a sum of Racah-normalized spherical harmonics  $C_{lm}(\theta, \phi)$  that fulfill condition  $C_{lm}(0, 0) = \delta_{m0}$  and  $R$ -dependent radial strengths or coefficients  $V_{l,m}(R)$ . For the icosahedral symmetry group this implies

$$V(R, \theta, \phi) = \sum_{l,m \in \mathcal{L}} V_{l,m}(R) \frac{C_{lm}(\theta, \phi) + C_{l-m}(\theta, \phi)}{2} \quad (1)$$

in our body-fixed coordinate system, where quantum numbers  $l, m$  are taken from the set  $\mathcal{L}$  with  $l = 0, 6, 10, 12, 16, 18, 20, \dots$  and non-negative  $m = 5n$  with  $n = 0, 1, 2, \dots$  and  $m \leq l$  [37–40]. In practice, the coefficients are obtained from a least squares fit to the *ab-initio* PES and we expand our potential with terms up to  $l = 20$  and  $m = 20$ . The strongest expansion coefficients  $V_{l,m}(R)$  as functions of  $R$  are shown in Fig. 3. The isotropic term  $V_{0,0}(R)$  dominates in the attractive part of the PES.

Atom-molecule collisional dynamics is often controlled by its van der Waals interactions. We have used the Casimir-Polder formula [41] to determine the relevant  $C_6$  van der Waals coefficients from dynamic polarizabilities of  $C_{60}$  and Ar as functions of imaginary frequencies. Our computation of the dynamic polarizability of  $C_{60}$  at its equilibrium geometry as functions of both real and imaginary frequency are described in Appendix A, while data for Ar have been taken from Ref. [42]. We find that the isotropic  $C_6$  coefficient is  $(2523 \pm 250)E_h a_0^6$ , whereas the anisotropic dispersion coefficients are negligibly small. Here,  $E_h$  is the Hartree energy. Small anisotropic dispersion coefficients might suggest that rotational quenching of  $^{12}C_{60}$  in collisions with Ar will have a very low probability of occurring. As we will show, however, when our two particles approach each other, other anisotropies induce small but non-negligible rotational transitions.

### III. ICOSAHEDRAL SYMMETRY ADAPTED ROTATIONAL STATES OF $C_{60}$

The icosahedral symmetry group  $I_h$  and Bose statistics among the sixty spinless  $^{12}C$  nuclei imply that only fully symmetric rotational wavefunctions  $|JM, K\rangle$  are allowed for the ground electronic-vibrational state with its zero total electron angular momentum [37–40]. These rotational states are eigenstates of the total angular momentum  $\mathbf{J}$  operator of  $^{12}C_{60}$  and its projection operator  $J_Z$  on the  $Z$  axis in a space-fixed coordinate system  $XYZ$  with corresponding quantum numbers  $J$  and  $M$ , respectively. Fully symmetric implies that

$$\hat{C}_i |JM, K\rangle = |JM, K\rangle \text{ and } \hat{I} \hat{C}_i |JM, K\rangle = |JM, K\rangle, \quad (2)$$

for all  $i = 1, \dots, 60$ , where the  $\hat{C}_i$  are the sixty rotations around the center of mass of  $^{12}C_{60}$  belonging to the rotational icosahedral group  $I$  and  $\hat{I}$  is the spatial inversion operator. For given  $J$  and  $M$ , index  $K = 1, \dots, N_h(J)$  labels the fully symmetric rotational wave functions. The number of allowed states,  $N_h(J)$ , has been computed *a priori* using group theory (See for example Ref. [38]), is either 0 or 1 for  $J < 30$ , and  $N_h(J) = N_h(J - 30) + 1$  for  $J \geq 30$ . In fact, we have  $N_h(J) = 1, 0, 0, 0, 0, 0, 1, 0, 0, 0, 1, 0, 1, 0$ , and 0 for  $J = 0, 1, \dots, 14$ , respectively, and  $N_h(J) = 1 - N_h(29 - J)$  for  $J < 30$ . The  $N_h(J)$  states correspond to the so-called superfine structure of  $^{12}C_{60}$ .

The general form of the unit-normalized rotational eigenstates is

$$|JM, K\rangle = \sum_{N=-J}^J a_{KN}^{(JM)} \sqrt{\frac{2J+1}{8\pi^2}} D_{MN}^{J*}(\phi_{\text{sf}}, \theta_{\text{sf}}, \varphi_{\text{sf}}), \quad (3)$$

where Wigner rotation matrices  $D_{MN}^J(\alpha, \beta, \gamma)$  are rigid rotor solutions that are eigenstates of  $J^2$ ,  $J_Z$ , and  $J_z$  with quantum numbers  $J$ ,  $M$ , and  $N$ , respectively [43]. Euler angles  $\phi_{\text{sf}}, \theta_{\text{sf}}, \varphi_{\text{sf}}$  orient the body-fixed  $xyz$  axes of  $^{12}C_{60}$ , defined in Sec. II, in the space-fixed  $XYZ$  coordinate system. Superscript  $*$  on the Wigner rotation matrices represents the complex conjugate.

The coefficients  $a_{KN}^{(JM)}$  for each pair  $J, M$  are uniquely determined by Eqs. (2). In fact, group theory states [38] that the coefficients  $a_{KN}^{(JM)}$  for fully symmetric rotational states are given by the  $N_h(J)$  linearly independent combinations of the  $2J + 1$  wavefunctions

$$\sum_{i=1}^{60} \mathcal{C}_i \sqrt{\frac{2J+1}{8\pi^2}} D_{M,N}^{J*}(\phi_{\text{sf}}, \theta_{\text{sf}}, \varphi_{\text{sf}}), \quad (4)$$

one for each  $N = -J, \dots, J$ . The sum in Eq. (4) is over all sixty rotation operators  $\mathcal{C}_i$  in the rotational icosahedral group and gives each Wigner rotation matrix equal weight. (These weights are the characters of the fully symmetric irreducible representation and we recall that  $N_h(J) \leq 2J + 1$ .) The action of a rotation  $\hat{C}_i$  on Wigner

functions is given by

$$\hat{C}_i D_{M,N}^{J*}(\phi_{sf}, \theta_{sf}, \varphi_{sf}) = \sum_{N'=-J}^J D_{M,N'}^{J*}(\phi_{sf}, \theta_{sf}, \varphi_{sf}) D_{N',N}^J(-\gamma_i, -\beta_i, -\alpha_i), \quad (5)$$

where  $\alpha_i, \beta_i, \gamma_i$  are the Euler angles describing the  $i$ -th rotation.

Finally, the inversion operator  $\mathcal{I}$  leaves Wigner rotation matrices unchanged up to phase factor  $(-1)^J$  and, thus, multiplies each term in Eq. (4) by a factor of two. We omitted this factor in the equation as it only changes the normalization. In practice, for each  $J, M$  we first construct all  $2J + 1$  states in Eq. (4) and then use singular value decomposition to determine all linearly independent (and orthonormal) states. Here, we rely on the list of Euler angles for the 60 rotations from Ref. [44], a rotation between our coordinate system and that of Ref. [44], and the numerical evaluation of Wigner rotation matrices, *e.g.*, see Refs. [45–47]. This enables us to independently verify the correct  $N_h(J)$ . When  $N_h(J) = 0$  for some of the  $J < 30$ , Eq. (4) is zero for all  $N$ .

We start our analysis of collision-induced excitation and quenching of rotational states of  $^{12}\text{C}_{60}$  in its ground vibrational state by studying the population distribution of rotational levels  $J$  of  $^{12}\text{C}_{60}$  for the three temperatures  $T = 100$  K, 150 K, and 300 K. The distributions are given by

$$p(J; T) = (2J + 1)N_h(J)e^{-BJ(J+1)/kT}/Z(T), \quad (6)$$

where  $B = hc \times 0.0028 \text{ cm}^{-1}$  is the rotational constant of  $^{12}\text{C}_{60}$  in its ground vibrational state, obtained from a fit to the experimental spectra in Refs. [29, 31],  $Z(T)$  is a normalization factor such that  $\sum_{J=0}^{\infty} p(J; T) = 1$ . For our study of collisional physics, we do not need to account for small energy shifts due to centrifugal distortions and the superfine structure of  $^{12}\text{C}_{60}$ .

Figure 4 shows distributions as functions of  $J$  for the three temperatures. We observe that for  $T = 150$  K angular momenta  $J$  up to  $\approx 350$  have significant occupation. In addition, for each temperature the figure shows the cases where the icosahedral symmetry of  $^{12}\text{C}_{60}$  is accounted for and one where the fullerene is modeled as a spherical top molecule, *i.e.*, where  $N_h(J)$  is replaced by  $2J + 1$ . The jagged distributions, when the icosahedral symmetry are accounted for, are a consequence of the complex degeneracy factor  $N_h(J)$  for the number of the allowed states at a given  $J$ . The jaggedness becomes less pronounced both with increasing quantum number  $J$  and increasing temperature and the curves approach the distribution of a rigid spherical top molecule.

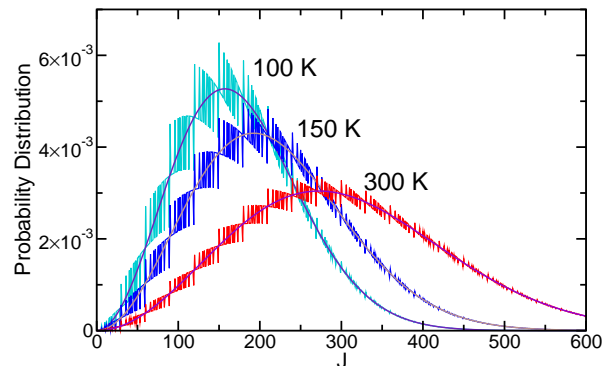


FIG. 4. Population or probability distributions of rotational levels  $J$  of the ground vibrational state of the  $^{12}\text{C}_{60}$  fullerene at temperatures of  $T = 100$  K (cyan curve), 150 K (blue curve) and 300 K (red curve). The smooth solid lines going through the center of jagged curves are rotational distributions that treat the  $^{12}\text{C}_{60}$  as a rigid spherical top, for which the degeneracy factor is  $(2J + 1)^2$  for each  $J$ .

#### IV. THEORY FOR CROSS SECTIONS FOR ROTATIONAL QUENCHING OF $\text{C}_{60}$ BY AR ATOMS

We use second-order perturbation theory (PT2) to compute inelastic cross sections for rotational transitions  $J, K \rightarrow J', K'$  averaged over both the direction  $\hat{k}$  of wave-vector  $\mathbf{k}$  in the relative motion of the  $^{12}\text{C}_{60}$ - $^{40}\text{Ar}$  system with reduced mass  $\mu$  and the initial projection  $M$  of the angular momentum  $J$  of  $^{12}\text{C}_{60}$  in its vibrational and electronic ground state. We account for both positive and negative values of quantum number  $K$  and, thereby, have not taken advantage of the parity symmetry inherent in the system. The zeroth-order Hamiltonian is defined by the relative motion of  $^{12}\text{C}_{60}$ - $^{40}\text{Ar}$  in the isotropic potential  $V_{0,0}(R)$ . This zeroth-order Hamiltonian conserves the relative orbital angular momentum or partial wave  $\ell$  between  $^{12}\text{C}_{60}$  and  $^{40}\text{Ar}$ . Within PT2, inelastic cross sections are then given by

$$\sigma_{J'K',JK}(E) = \frac{1}{4\pi} \int d\hat{k} \frac{1}{2J+1} \sum_{MM'} \frac{2\pi}{\hbar} \times \sum_{\ell'=0}^{\infty} \sum_{m'=-\ell'}^{\ell'} |\langle \psi_{JM,K}^{\mathbf{k}} | V(R, \theta, \phi) | \psi_{\ell'm',J'M'K'}^E \rangle|^2, \quad (7)$$

where

$$|\psi_{JM,K}^{\mathbf{k}}\rangle = 4\pi \sqrt{\frac{\mu}{\hbar k}} |JM, K\rangle \sum_{\ell=0}^{\infty} i^{\ell} f_{\ell k}(R) \left( Y_{\ell}(\hat{k}) \cdot Y_{\ell}(\hat{R}) \right) \quad (8)$$

are unit flux normalized, zeroth-order radial wavefunctions and

$$|\psi_{\ell m, JMK}^E\rangle = |JM, K\rangle \sqrt{\frac{2k\mu}{\pi \hbar^2}} f_{\ell k}(R) Y_{\ell m}(\hat{R}) \quad (9)$$

are energy normalized, zeroth-order radial wavefunctions. Furthermore, kets  $|JM, K\rangle$  are defined by Eq. (3),  $Y_{\ell m}(\hat{x})$  are unit-normalized spherical harmonic functions, and  $f_{\ell k}(R)$  are solutions of the radial Schrödinger equation

$$\left(-\frac{\hbar^2}{2\mu} \frac{d^2}{dR^2} + \frac{\hbar^2 \ell(\ell+1)}{2\mu R^2} + V_{0,0}(R)\right) f_{\ell k}(R) = E f_{\ell k}(R), \quad (10)$$

with kinetic energy  $E = \hbar^2 k^2 / (2\mu)$ , partial wave  $\ell$ , and asymptotic behavior

$$f_{\ell k}(R) \rightarrow \frac{1}{k} \sin(kR - \pi\ell/2 + \eta_\ell(k)) \quad (11)$$

for  $R \rightarrow \infty$ . Here,  $\eta_\ell(k)$  are phase shifts.

After integration over  $\hat{k}$  Eq. (7) becomes

$$\sigma_{J'K', JK}(E) = \frac{1}{2\hbar} \frac{1}{2J+1} \sum_{MM'} \sum_{\ell, \ell'=0}^{\infty} \sum_{m=-\ell}^{\ell} \sum_{m'=-\ell'}^{\ell'} \left| \left\langle \psi_{\ell m, JMK}^{(1)} | V(R, \theta, \phi) | \psi_{\ell' m', J'M'K'}^E \right\rangle \right|^2, \quad (12)$$

where

$$\psi_{\ell m, JMK}^{(1)} = 4\pi \sqrt{\frac{\mu}{\hbar k}} |JM, K\rangle i^\ell f_{\ell k}(R) Y_{\ell m}(\hat{R}). \quad (13)$$

Note that  $m+M = m'+M'$  is conserved in the collision.

Rather than numerically solving Eq. (10) by a finite difference method, we solve this equation using a discrete variable representation (DVR) [48] to discretize the differential operator  $d^2/dR^2$  on radial interval  $[R_{\min}, R_{\max}]$  with  $R_{\min} = 11a_0$ ,  $R_{\max} = 1000a_0$ , and discretization step  $\delta R = 0.1a_0$ . In the DVR representation,  $f_{\ell k}^{\text{DVR}}(R_{\min}) = f_{\ell k}^{\text{DVR}}(R_{\max}) = 0$  and we find a set of discrete energies  $E$  that satisfy these conditions by solving the relevant eigenvalue problem for each  $\ell$ . The unit-normalized eigensolutions  $f_{\ell k}^{\text{DVR}}(R)$  are converted to wavefunctions with normalization given in Eq. (11) using

$$f_{\ell k}(R) = \frac{1}{k} \sqrt{\frac{R_{\max}}{2}} f_{\ell k}^{\text{DVR}}(R). \quad (14)$$

Matrix elements in Eq. (12) at arbitrary  $E$  can be found by interpolation. We have included several hundreds of partial waves  $\ell$  to reach convergence within our perturbation theory.

## V. COLLISION-INDUCED QUENCHING AND REPOPULATION

In this section, we present perturbative results for rotational inelastic rate coefficient

$$K_{J', J}(E) = \frac{1}{N_h(J)} \sum_{K=1}^{N_h(J)} \sum_{K'=1}^{N_h(J')} \sum v \sigma_{J'K', JK}(E), \quad (15)$$

where relative velocity  $v = \hbar k / \mu$ . Figure 5 shows perturbative inelastic rate coefficients at collision energy  $E = k \times 150$  K for sequential initial angular momenta  $J_{\text{ini}}$  of  $^{12}\text{C}_{60}$  between 60 and 67 as functions of outgoing and final angular momenta  $J_{\text{out}} \neq J_{\text{ini}}$ . We have only included the contributions from the strongest expansion coefficients  $V_{l,m}(R)$  of the interaction potential  $V(R, \theta, \varphi)$  shown in Fig. 3. Hence, the outgoing angular momentum satisfies  $J_{\text{ini}} - 10 \leq J_{\text{out}} \leq J_{\text{ini}} + 10$ . We also observe that rate coefficients have a non-monotonic, seemingly random behavior as functions of  $J_{\text{out}}$  around a value just under  $2 \times 10^{-11} \text{ cm}^3/\text{s}$  both for  $J_{\text{out}} < J_{\text{ini}}$  corresponding to rotational de-excitation and for  $J_{\text{out}} > J_{\text{ini}}$  corresponding to rotational excitation. In fact, no obvious pattern from one initial angular momentum to another exists. The complex behavior is due to the  $I_h$  symmetry of  $^{12}\text{C}_{60}$ .

Figure 6 shows perturbative rate coefficients at collision energy  $E = k \times 150$  K for initial angular momenta  $J_{\text{ini}} = 60, 150, \text{ and } 220$  spanning the relevant significantly populated angular momenta at temperature  $T = 150$  K. Several observations can be made. Firstly, the amplitude of the ‘‘random’’ behavior of the rate coefficients is smaller for larger  $J_{\text{ini}}$ . Secondly, the pattern as function of  $J_{\text{out}} - J_{\text{ini}}$  is very similar for the three  $J_{\text{ini}}$  with the largest rate coefficients occurring for  $|J_{\text{out}} - J_{\text{ini}}| = 5$ .

The elastic rate coefficients with  $J_{\text{out}} = J_{\text{ini}}$  at the same collision energy (not shown) are more than a hundred times larger and within our approximate approach derived for scattering from the isotropic potential  $V_{0,0}(R)$  and, thus, phase shifts  $\eta_\ell(k)$ . In fact, this elastic rate coefficient is very close to its semi-classical value from Ref. [49] given by

$$K_{\text{elast}}(E) = 6.125 \dots \left(\frac{E}{E_6}\right)^{3/10} \frac{\hbar x_6}{\mu}, \quad (16)$$

where van der Waals energy  $E_6 = \hbar^2 / (2\mu x_6^2)$  and van der Waals length  $x_6 = \sqrt[4]{2\mu C_6 / \hbar^2}$ . See, for example, Ref. [50] for a comparison of thermalized total elastic rate coefficients using quantum simulations and the semi-classical model. For our system,  $E_6 \approx k \times 0.12$  mK and  $\hbar x_6 / \mu \approx 1.2 \times 10^{-11} \text{ cm}^3/\text{s}$ , so that  $K_{\text{elast}}(E) \approx 5.0 \times 10^{-9} \text{ cm}^3/\text{s}$  at  $E/k = 150$  K. In other words, inelastic rate coefficients are small, validating our perturbative procedure for these rate coefficients.

Finally, Fig. 7 shows the mean and spread of collision-induced inelastic rate coefficients between  $^{12}\text{C}_{60}$  and  $^{40}\text{Ar}$  as a function of initial angular momentum  $J_{\text{ini}}$  of  $^{12}\text{C}_{60}$  at collision energies  $k \times 100$  K and  $k \times 150$  K. Within our perturbative calculations, these quantities are defined as

$$\mathcal{K}_J(E) = \frac{1}{20} \sum_{J'=J-10, J' \neq J}^{J+10} K_{J', J}(E) \quad (17)$$

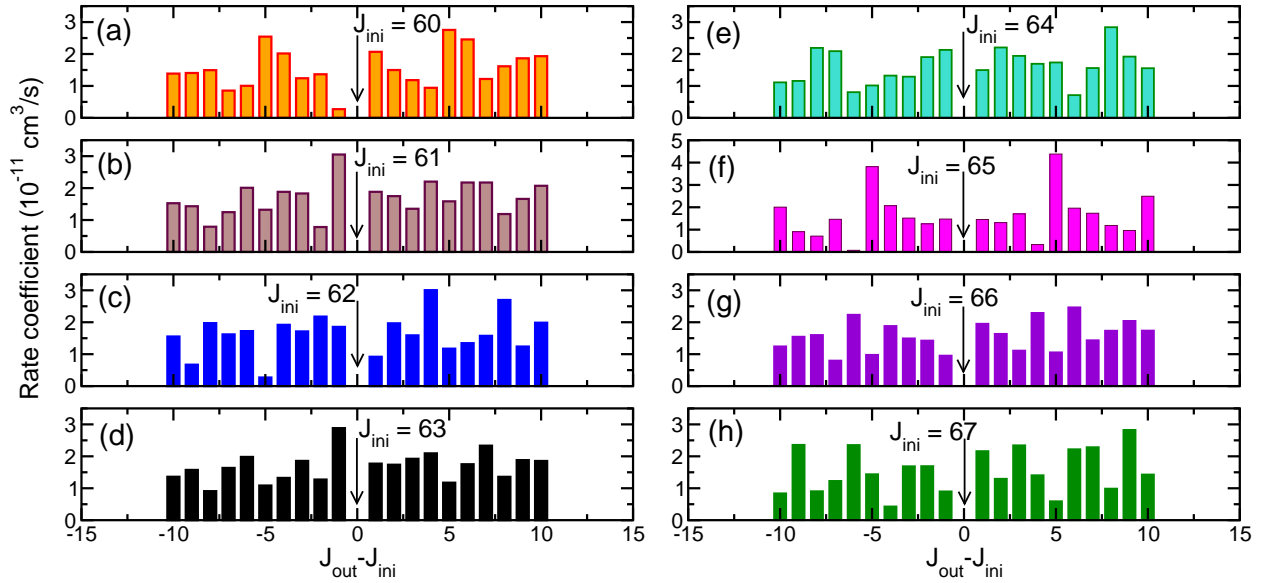


FIG. 5. Collision-induced quenching and repopulation rate coefficients of rotational levels  $J_{\text{ini}}$  of  $^{12}\text{C}_{60}$  between 60 and 67 (panels (a) through (h)) with  $^{40}\text{Ar}$  as functions of the final rotational state  $J_{\text{out}}$  at collisional energy  $E = k \times 150$  K. The vertical axes are the same for all panels except that for panel (f).

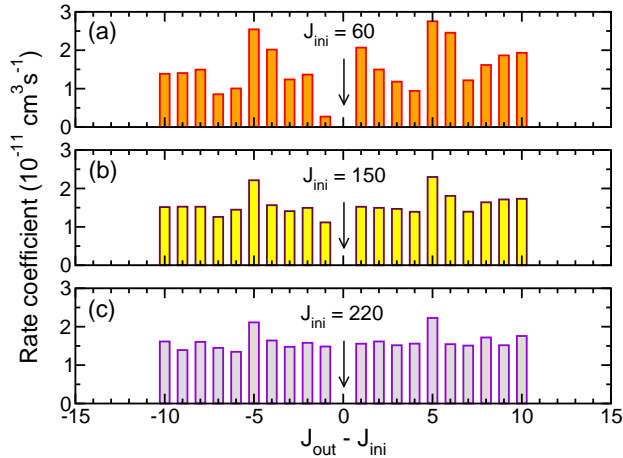


FIG. 6. Collision-induced inelastic rate coefficients of initial rotational levels  $J_{\text{ini}} = 60, 150,$  and  $220$  of  $^{12}\text{C}_{60}$  (panels (a), (b), and (c), respectively) with  $^{40}\text{Ar}$  as functions of the final rotational state  $J_{\text{out}}$  at collision energy  $k \times 150$  K.

and

$$u_J(E) = \sqrt{\frac{1}{20} \sum_{J'=J-10, J' \neq J}^{J+10} (\mathcal{K}_{J',J}(E) - \mathcal{K}_J(E))^2}, \quad (18)$$

respectively. We note that  $\mathcal{K}_{J_{\text{ini}}}(E)$  and  $u_{J_{\text{ini}}}(E)$  have only been computed for a limited set of  $J_{\text{ini}}$  due to the combined complexity of computing symmetry-adapted states  $|JM, K\rangle$ , eigensolutions  $f_{\ell k}(R)$ , matrix elements of potentials  $V_{l,m}(R)$ , and summing over initial and final

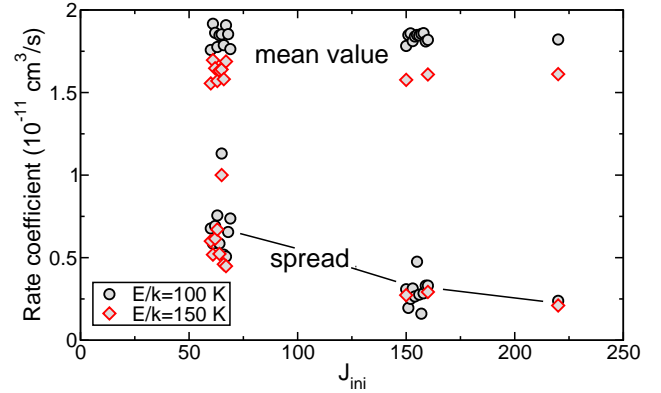


FIG. 7. The mean and spread of  $^{12}\text{C}_{60}$ - $^{40}\text{Ar}$  collision-induced inelastic rate coefficients as function of initial rotational level  $J_{\text{ini}}$  of  $^{12}\text{C}_{60}$  at collision energies  $k \times 100$  K (black circles) and  $k \times 150$  K (red diamonds). The mean and spread have been computed with respect to final rotational state  $J_{\text{out}}$ .

partial wave  $\ell$  and  $\ell'$  and all projection quantum numbers.

We also observe that mean  $\mathcal{K}_{J_{\text{ini}}}(E)$  has small, seemingly random variations from one  $J_{\text{ini}}$  to the next that become smaller for increasing  $J_{\text{ini}}$  as best observed for the data at  $E = k \times 100$  K. Still the mean is mostly independent of  $J_{\text{ini}}$  over a larger range of  $J_{\text{ini}}$ , *i.e.*, those relevant for our temperatures. Finally, the mean value slowly decreases with  $E$  for energies around  $k \times 100$  K and  $k \times 150$  K. The spread  $u_{J_{\text{ini}}}(E)$  also has small, random variations from one  $J_{\text{ini}}$  to the next, but is observably getting smaller over larger ranges of  $J_{\text{ini}}$ . The spread

$u_{J_{\text{ini}}}(E)$  is larger than the variation in mean  $\mathcal{K}_{J_{\text{ini}}}(E)$  from one  $J_{\text{ini}}$  to the next.

Our observations regarding the weak dependence of  $\mathcal{K}_J(E)$  and  $u_J(E)$  on energy  $E$  and  $^{12}\text{C}_{60}$  rotational state  $J$  in Fig. 7 enable an estimate of thermalized rate coefficients for each  $J$  and temperatures between 100 K and 150 K. We assume  $\langle \mathcal{K}_J(T) \rangle \approx \mathcal{K}_J(E = kT)$  and we find typical thermalized inelastic rate coefficients of just under  $2 \times 10^{-11} \text{ cm}^3/\text{s}$ .

For typical datasets used in Ref. [30], the Ar number density was  $n_{\text{Ar}} = 1.6 \times 10^{16} \text{ cm}^{-3}$ , which leads to a time scale  $\tau_{\text{inelas}} \approx 3 \mu\text{s}$  for removing population from total angular momentum  $J_{\text{ini}}$  of  $^{12}\text{C}_{60}$  due to collisions with argon atoms. This time scale, however, cannot be directly compared to time scales measured in experiments by Ref. [30] implementing the setup in Fig. 1. Such a model must account for laser beams with millimeter beam waists,  $\text{C}_{60}$  molecules diffusing in and out of these beams, and the mean free path for elastic  $\text{C}_{60}$ -Ar collisions given by  $\langle v \rangle / [\langle K_{\text{elast}}(E) \rangle n_{\text{Ar}}] \approx 4 \mu\text{m}$  at  $T = 150 \text{ K}$ . Here, the thermalized relative velocity  $\langle v \rangle$  is given by  $\langle v \rangle = (2/\sqrt{\pi})\sqrt{2kT/\mu}$ . We might expect that the observed time scale will be many times  $\tau_{\text{inelas}}$ . This modeling falls outside the scope of this paper.

## VI. SUMMARY

We have described rotationally inelastic collisions of the  $^{12}\text{C}_{60}$  molecule with inert  $^{40}\text{Ar}$  for gas temperatures near 150 K. At these temperature, we can concentrate on the thermal population of hundreds of rotational levels of the  $v = 0$  vibrational state of  $^{12}\text{C}_{60}$  in its electronic ground state. We summarized a calculation of the anisotropic terms in the interaction potential energy surface of the system, described internal rotational states of  $\text{C}_{60}$  in terms of its icosahedral symmetry, and performed second-order perturbative quantum calculations of the rotationally inelastic inelastic rate coefficients. The inelastic rate coefficients are found to be order of magnitude smaller than the elastic rate coefficients.

## ACKNOWLEDGEMENTS

SK, AL, and JK acknowledges funding by the AFOSR, Grant No. FA9550-21-1-0153, National Science Foundation, Grant No. PHY-2409425, and the Gordon and Betty Moore Foundation, Grant No. GBMF12330.

### Appendix A: Dipole polarizability of $\text{C}_{60}$ and van der Waals coefficient for $\text{C}_{60}$ -Ar

The  $\text{C}_{60}$  molecule in its electronic and vibrational ground state has a high symmetry and many of the lowest multipole moments vanish. For example, dipole or quadrupole moments are zero. The dipole polarizability

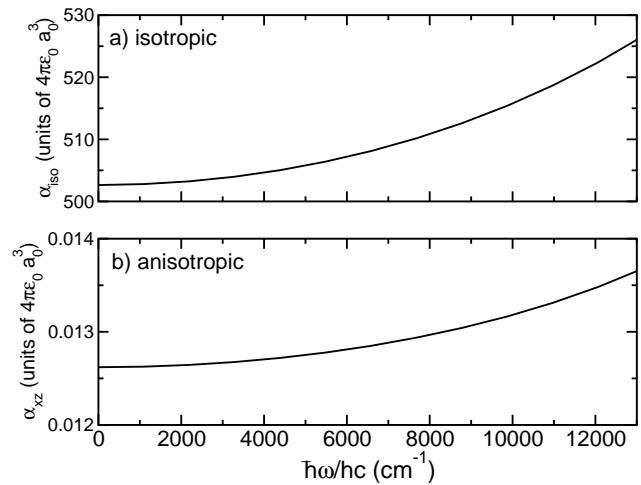


FIG. 8. Scaled isotropic  $\alpha_{\text{iso}}(\omega)$  (panel a) and anisotropic  $\alpha_{xz}(\omega)$  (panel b) dynamic polarizability of  $\text{C}_{60}$  as functions of laser frequency  $\omega$ .

tensor  $\alpha_{ab}(\omega)$  with  $a, b = x, y,$  and  $z$  in the body-fixed coordinate system and laser frequency  $\omega$  or a photon energy  $\hbar\omega$ , however, is non-zero. The isotropic dipole polarizability is defined by  $\alpha_{\text{iso}}(\omega) \equiv \sum_a \alpha_{aa}(\omega)/3$ .

The isotropic, static dipole polarizability  $\alpha_{\text{iso}}(0)$  of the fullerene in its electronic and vibrational ground state has been extensively studied both experimentally and theoretically. A recent experimental value is  $4\pi\epsilon_0 \times 590(17)a_0^3$  [51], where the number in parentheses is the standard uncertainty in the last two digits and  $\epsilon_0$  is the vacuum electric permittivity. A recent theoretical value of  $4\pi\epsilon_0 \times 545.3a_0^3$  including a small contribution from zero-point vibrational motion was published in Ref. [52]. Significant differences in values for  $\alpha_{\text{iso}}(0)$  with a spread larger than the experimental uncertainty of Ref. [51] among the published experimental and theoretical evaluations, however, exists.

In Ref. [30] we calculated the static dipole polarizability tensor of  $\text{C}_{60}$  using density functional theory in the Q-Chem program with the 6-311G(d,p) basis and Perdew-Becke functionals [53, 54]. The calculations lead to  $\alpha_{\text{iso}}(0) = 4\pi\epsilon_0 \times 502.6420a_0^3$ , a value that is at the lower end of the published theoretical values. In addition, we derived a small anisotropy of the static polarizability tensor of  $\kappa(0) = 3.5 \times 10^{-6}$  defined via

$$\kappa^2(\omega) = \frac{1}{6} \sum_a \left( \frac{\alpha_{aa}(\omega) - \alpha_{\text{iso}}(\omega)}{\alpha_{\text{iso}}(\omega)} \right)^2 \quad (\text{A1})$$

for any frequency  $\omega$ .

In order to estimate the  $C_6$  dispersion coefficient for the  $\text{C}_{60}$ -Ar system, we also calculated the frequency-dependent dipole polarizability tensor using the coupled-cluster propagator implemented in the MOLPRO program [55] with single and double excitations (CCSD) and the minimal STO-3G basis due to computational lim-

itations These calculations were performed up to  $\hbar\omega = hc \times 13\,000\text{ cm}^{-1}$  beyond which the coupled-cluster propagator did not converge. For each tensor component, the frequency-dependent results for the dipole polarizability are then scaled to coincide with the corresponding static dipole polarizability tensor components obtained by our Q-Chem calculations with its larger basis set. These scaled data are shown in Fig. 8 as function of frequency  $\omega$ . The dynamic dipole polarizability has a singularity at a photon energy  $\Delta > hc \times 13\,000\text{ cm}^{-1}$  corresponding to

a transition to an electronically excited state of  $C_{60}$ .

We fit the dynamic dipole polarizability to the functional form  $\alpha_{ab}(\omega) = \alpha_{ab}(0)\Delta^2/[\Delta^2 - (\hbar\omega)^2]$  with adjustable parameters  $\alpha_{ab}(0)$  and  $\Delta$  and use  $\alpha_{ab}(i\omega)$  at imaginary frequencies  $i\omega$  with the dipole polarizability of the Ar atom at imaginary frequencies from Ref. [42] in the Casimir-Polder formula [56], to find that the isotropic  $C_6$  dispersion coefficient is  $2523E_h a_0^6$ . We estimate that this dispersion coefficient has a standard uncertainty of 10%. The anisotropic dispersion coefficients are effectively zero.

- 
- [1] H. W. Kroto, J. R. Heath, S. C. O'Brien, R. F. Curl, and R. E. Smalley, "C<sub>60</sub>: Buckminsterfullerene," *Nature* **318**, 162–163 (1985).
- [2] W. Krätschmer, L. D. Lamb, K. Fostiropoulos, and D. R. Huffman, "Solid C<sub>60</sub>: A new form of carbon," *Nature* **347**, 354–358 (1990).
- [3] M.S. Dresselhaus, G.D. Dresselhaus, and P.C. Eklund, *Science of Fullerenes and Carbon Nanotubes* (Academic Press, London, 1996).
- [4] A. Kausar, "Breakthroughs of fullerene in optoelectronic devices—an overview," *Hybrid Adv.* **6**, 100233 (2024).
- [5] W. I. F. David, R. M. Ibberson, J. C. Matthewman, K. Prassides, T. J. S. Dennis, J. P. Hare, H. W. Kroto, R. Taylor, and D. R. M. Walton, "Crystal structure and bonding of ordered C<sub>60</sub>," *Nature* **353**, 147–149 (1991).
- [6] J. R. Heath, S. C. O'Brien, Q. Zhang, Y. Liu, R. F. Curl, F. K. Tittel, and R. E. Smalley, "Lanthanum complexes of spheroidal carbon shells," *J. Am. Chem. Soc.* **107**, 7779–7780 (1985).
- [7] K. Kurotobi and Y. Murata, "A single molecule of water encapsulated in fullerene C<sub>60</sub>," *Science* **333**, 613–616 (2011).
- [8] Z. Bačić, "Perspective: Accurate treatment of the quantum dynamics of light molecules inside fullerene cages: Translation-rotation states, spectroscopy, and symmetry breaking," *J. Chem. Phys.* **149**, 100901 (2018).
- [9] S. P. Jarvis, H. Sang, F. Junqueira, O. Gordon, J. E. A. Hodgkinson, A. Saywell, P. Rahe, S. Mamone, S. Taylor, A. Sweetman, J. Leaf, D. A. Duncan, T.-L. Lee, P. K. Thakur, G. Hoffman, R. J. Whitby, M. H. Levitt, G. Held, L. Kantorovich, P. Moriarty, and R. G. Jones, "Chemical shielding of H<sub>2</sub>O and HF encapsulated inside a C<sub>60</sub> cage," *Commun. Chem.* **4**, 135 (2021).
- [10] A. A. Popov, S. Yang, and L. Dunsch, "Endohedral fullerenes," *Chem. Rev.* **113**, 5989–6113 (2013).
- [11] V. K. Vyas, G. R. Bacanu, M. Soundararajan, E. S. Marsden, T. Jafari, A. Shugai, M. E. Light, U. Nagel, T. Rõöm, M. H. Levitt, and R. J. Whitby, "Squeezing formaldehyde into C<sub>60</sub> fullerene," *Nat. Commun.* **15**, 2515 (2024).
- [12] T. Jafari, A. Shugai, U. Nagel, E. S. Marsden, S. Bloodworth, G. Hoffman, G. R. Bacanu, M. C. Walkey, M. H. Levitt, R. J. Whitby, and T. Rõ om, "Terahertz spectroscopy study of the confining potential for methane in the endofullerene CH<sub>4</sub>@C<sub>60</sub>," *J. Chem. Phys.* **163**, 084308 (2025).
- [13] S.-Y. Xie, F. Gao, X. Lu, R.-B. Huang, C.-R. Wang, X. Zhang, M.-L. Liu, S.-L. Deng, and L.-S. Zheng, "Capturing the labile fullerene[50] as C<sub>50</sub>Cl<sub>10</sub>," *Science* **304**, 699–699 (2004).
- [14] Q.-H. Weng, Q. He, T. Liu, H.-Y. Huang, J.-H. Chen, Z.-Y. Gao, S.-Y. Xie, X. Lu, R.-B. Huang, and L.-S. Zheng, "Simple combustion production and characterization of octahydro[60]fullerene with a non-IPR C<sub>60</sub> cage," *J. Am. Chem. Soc.* **132**, 15093–15095 (2010).
- [15] S. Filippone and N. Martín, "Exohedral fullerenes," in *Encyclopedia of Polymeric Nanomaterials*, edited by S. Kobayashi and K. Müllen (Springer Berlin Heidelberg, Berlin, Heidelberg, 2021) pp. 1–16.
- [16] J. S. Tsai, "C<sub>60</sub> and its superconducting properties," *IEEE Trans. Magn.* **8**, 434–439 (1993).
- [17] A. P. Ramirez, "Superconductivity in alkali-doped C<sub>60</sub>," *Physica C* **514**, 166–172 (2015), in Special issue on Superconducting Materials: Conventional, Unconventional and Undetermined.
- [18] C. B. Winkelmann, N. Roch, W. Wernsdorfer, V. Bouchiat, and F. Balestro, "Superconductivity in a single-C<sub>60</sub> transistor," *Nat. Phys.* **5**, 876–879 (2009).
- [19] L. B. Tuli, S. J. Goettl, A. M. Turner, A. H. Howlader, P. Hemberger, S. F. Wnuk, T. Guo, A. M. Mebel, and R. I. Kaiser, "Gas phase synthesis of the C<sub>40</sub> nano bowl C<sub>40</sub>H<sub>10</sub>," *Nat. Commun.* **14**, 1527 (2023).
- [20] G. H. Herbig, "The diffuse interstellar bands. The region 4400 - 6850 Å," *Astrophys. J.* **196**, 129–160 (1975).
- [21] A. Leger and J. L. Puget, "Identification of the Unidentified Infrared Emission Features of Interstellar Dust," *A & A* **137**, L5–L8 (1984).
- [22] A. Leger and L. D'Hendecourt, "Identification of Polycyclic Aromatic Hydrocarbons," in *Astrochemistry*, IAU Symposium, Vol. 120, edited by M. S. Vardya and S. P. Tarafdar (1987) p. 557.
- [23] A. Leger, "On the Presence of Large Aromatic Molecules in the Interstellar Medium Inferred from Infrared Data," in *Protostars and Molecular Clouds*, edited by T. Montmerle and C. Bertout (1987) p. 77.
- [24] G. H. Herbig, "The search for interstellar C<sub>60</sub>," *ApJ* **542**, 334–343 (2000).
- [25] J. Cami, J. Bernard-Salas, E. Peeters, and S. E. Malek, "Detection of C<sub>60</sub> and C<sub>70</sub> in a young planetary nebula," *Science* **329**, 1180–1182 (2010).
- [26] Y. Zhang and S. Kwok, "On the detections of C<sub>60</sub> and derivatives in circumstellar environments," *Earth, Planets Sp.* **65**, 1069–1081 (2013).
- [27] A. Omont, "Interstellar fullerene compounds and diffuse

- interstellar bands,” *A&A* **590**, A52 (2016).
- [28] M. Feng and J. Twamley, “Selective pulse implementation of two-qubit gates for spin- $\frac{3}{2}$ -based fullerene quantum-information processing,” *Phys. Rev. A* **70**, 032318 (2004).
- [29] P. Bryan Changala, Marissa L. Weichman, Kevin F. Lee, Martin E. Fermann, and Jun Ye, “Rovibrational quantum state resolution of the C<sub>60</sub> fullerene,” *Science* **363**, 49–54 (2019).
- [30] L. R. Liu, P. B. Changala, M. L. Weichman, Q. Liang, J. Toscano, J. Klos, S. Kotochigova, D. J. Nesbitt, and J. Ye, “Collision-induced C<sub>60</sub> rovibrational relaxation probed by state-resolved nonlinear spectroscopy,” *PRX Quantum* **3**, 030332 (2022).
- [31] L. R. Liu, D. Rosenberg, P. B. Changala, P. J. D. Crowley, D. J. Nesbitt, N. Y. Yao, T. V. Tschersbul, and J. Ye, “Ergodicity breaking in rapidly rotating C<sub>60</sub> fullerenes,” *Science* **381**, 778–783 (2023).
- [32] Y.-C. Chan, L. R. Liu, A. Scheck, D. J. Nesbitt, J. Ye, and D. Rosenberg, “Full confirmation of icosahedral Bose-Einstein statistics in cold <sup>12</sup>C<sub>60</sub>,” *Phys. Rev. Res.* **7**, L032029 (2025).
- [33] L. R. Liu and J. Ye, “Quantum state-resolved structure and dynamics of C<sub>60</sub> fullerenes,” *Annu. Rev. Phys. Chem.* **76**, 303–328 (2025).
- [34] A. M. Vassallo, L. S. K. Pang, P. A. Cole-Clarke, and M. A. Wilson, “Emission FTIR study of C<sub>60</sub> thermal stability and oxidation,” *J. Am. Chem. Soc.* **113**, 7820–7821 (1991).
- [35] M. J. Frisch, G. W. Trucks, H. B. Schlegel, G. E. Scuseria, M. A. Robb, J. R. Cheeseman, G. Scalmani, V. Barone, B. Mennucci, G. A. Petersson, H. Nakatsuji, M. Caricato, X. Li, H. P. Hratchian, A. F. Izmaylov, J. Bloino, G. Zheng, J. L. Sonnenberg, M. Hada, M. Ehara, K. Toyota, R. Fukuda, J. Hasegawa, M. Ishida, T. Nakajima, Y. Honda, O. Kitao, H. Nakai, T. Vreven, J. A. Montgomery, Jr., J. E. Peralta, F. Ogliaro, M. Bearpark, J. J. Heyd, E. Brothers, K. N. Kudin, V. N. Staroverov, T. Keith, R. Kobayashi, J. Normand, K. Raghavachari, A. Rendell, J. C. Burant, S. S. Iyengar, J. Tomasi, M. Cossi, N. Rega, J. M. Millam, M. Klene, J. E. Knox, J. B. Cross, V. Bakken, C. Adamo, J. Jaramillo, R. Gomperts, R. E. Stratmann, O. Yazyev, A. J. Austin, R. Cammi, C. Pomelli, J. W. Ochterski, R. L. Martin, K. Morokuma, V. G. Zakrzewski, G. A. Voth, P. Salvador, J. J. Dannenberg, S. Dapprich, A. D. Daniels, O. Farkas, J. B. Foresman, J. V. Ortiz, J. Cioslowski, and D. J. Fox, “*Gaussian 09, Revision E.01*,” (2013), Gaussian, Inc., Wallingford CT.
- [36] S. Tsuzuki and T. Uchimaru, “Accuracy of intermolecular interaction energies, particularly those of heteroatom containing molecules obtained by DFT calculations with Grimme’s D2, D3 and D3BJ dispersion corrections,” *Phys. Chem. Chem. Phys.* **22**, 22508–22519 (2020).
- [37] W. G. Harter and D. E. Weeks, “Rovibrational spectral fine structure of icosahedral molecules,” *Chem. Phys. Lett.* **132**, 387–392 (1986).
- [38] W. G. Harter and D. E. Weeks, “Rotation–vibration spectra of icosahedral molecules. I. Icosahedral symmetry analysis and fine structure,” *J. Chem. Phys.* **90**, 4727–4743 (1989).
- [39] R. Saito, G. Dresselhaus, and M. S. Dresselhaus, “Hindered rotation of solid <sup>12</sup>C<sub>60</sub> and <sup>13</sup>C<sub>60</sub>,” *Phys. Rev. B* **50**, 5680–5688 (1994).
- [40] P. R. Bunker and P. Jensen, “Spherical top molecules and the molecular symmetry group,” *Mol. Phys.* **97**, 255–264 (1999).
- [41] H. B. G. Casimir and D. Polder, “The influence of retardation on the London-van der Waals forces,” *Phys. Rev.* **73**, 360–372 (1948).
- [42] Andrei Derevianko, Sergey G. Porsev, and James F. Babb, “Electric dipole polarizabilities at imaginary frequencies for hydrogen, the alkali-metal, alkaline-earth, and noble gas atoms,” *At. Data Nucl. Data Tables* **96**, 323–331 (2010).
- [43] D. M. Brink and G. R. Satchler, *Angular Momentum*, 3rd ed. (Clarendon Press, Oxford, 1993).
- [44] E. Martinez-Torres, J. J. Lopez-Gonzalez, M. Fernandez-Gomez, and A. Cardenete-Espinosa, “Icosahedral matrix representations as a function of Eulerian angles,” *J. Chem. Educ.* **66**, 706 (1989).
- [45] H. Dachsels, “Fast and accurate determination of the Wigner rotation matrices in the fast multipole method,” *J. Chem. Phys.* **124**, 144115 (2006).
- [46] N. Tajima, “Analytical formula for numerical evaluations of the Wigner rotation matrices at high spins,” *Phys. Rev. C* **91**, 014320 (2015).
- [47] B.-L. Wang, F. Gao, L.-J. Wang, and Y. Sun, “Effective and efficient algorithm for the Wigner rotation matrix at high angular momenta,” *Phys. Rev. C* **106**, 054320 (2022).
- [48] D. T. Colbert and W. H. Miller, “A novel discrete variable representation for quantum mechanical reactive scattering via the S-matrix Kohn method,” *J. Chem. Phys.* **96**, 1982–1991 (1992).
- [49] M. S. Child, *Molecular Collision Theory* (Academic Press, London and New York, 1974).
- [50] J. Klos and E. Tiesinga, “Elastic and glancing-angle rate coefficients for heating of ultracold Li and Rb atoms by collisions with room-temperature noble gases, H<sub>2</sub>, and N<sub>2</sub>,” *J. Chem. Phys.* **158**, 014308 (2023).
- [51] Y. Y. Fein, P. Geyer, F. Kialka, S. Gerlich, and M. Arndt, “Improved accuracy fullerene polarizability measurements in a long-baseline matter-wave interferometer,” *Phys. Rev. Res.* **1**, 033158 (2019).
- [52] K. U. Lao, Y. Yang, and R. A. DiStasio, “Electron confinement meet electron delocalization: non-additivity and finite-size effects in the polarizabilities and dispersion coefficients of the fullerenes,” *Phys. Chem. Chem. Phys.* **23**, 5773–5779 (2021).
- [53] John P. Perdew, “Density-functional approximation for the correlation energy of the inhomogeneous electron gas,” *Phys. Rev. B* **33**, 8822–8824 (1986).
- [54] A. D. Becke, “Density-functional exchange-energy approximation with correct asymptotic behavior,” *Phys. Rev. A* **38**, 3098–3100 (1988).
- [55] H.-J. Werner, P. J. Knowles, G. Knizia, F. R. Manby, M. Schütz, P. Celani, W. Györfy, D. Kats, T. Korona, R. Lindh, A. Mitrushenkov, G. Rauhut, K. R. Shamasundar, T. B. Adler, R. D. Amos, S. J. Bennie, A. Bernhardsson, A. Berning, D. L. Cooper, M. J. O. Deegan, A. J. Dobbyn, F. Eckert, E. Goll, C. Hampel, A. Hesselmann, G. Hetzer, T. Hrenar, G. Jansen, C. Köppl, S. J. R. Lee, Y. Liu, A. W. Lloyd, Q. Ma, R. A. Mata, A. J. May, S. J. McNicholas, W. Meyer, T. F. Miller III, M. E. Mura, A. Nicklass, D. P. O’Neill, P. Palmieri, D. Peng, K. Pflüger, R. Pitzer, M. Reiher, T. Shiozaki, H. Stoll, A. J. Stone, R. Tarroni, T. Thorsteinsson, M. Wang, and

M. Welborn, “Molpro, version 2015.1, a package of ab initio programs,” (2015).

[56] A. Stone, *The theory of intermolecular forces*, 2nd ed. (Oxford University Press, 2013).